20. Yang, P. *et al.* Mirrorless lasing from mesostructured waveguides patterned by soft lithography. *Science* **287,** 465–467 (2000).
21. Chang, S.-C. *et al.* Multicolor organic light-emitting diodes processed by hybrid inkjet printing. *Adv. Mater.* **11,** 734–737 (1999).
22. Pede, D., Serra, G. & De Rossi, D. Microfabrication of conducting polymer devices by ink-jet stereolithography. *Mater. Sci. Eng. C.* **5,** 289–291 (1998).
23. Lu, Y. *et al.* Aerosol-assisted self-assembly of spherical, silica nanoparticles exhibiting hexagonal, cubic and vesicular mesophases. *Nature* **398,** 223–226 (1999).
24. Wilbur, J. L., Kumar, A., Biebuyck, H. A., Kim, E. & Whitesides, G. M. Microcontact printing of self-assembled monolayers: applications in microfabrication. *Nanotechnology* **7,** 452–457 (1996).
25. Tender, L. M., Worley, R. L., Fan, H. & Lopez, G. P. Electrochemical patterning of self-assembled monolayers onto microscopic arrays of gold electrodes fabricated by laser ablation. *Langmuir* **12,** 5515–5518 (1996).
26. Douglas Frink, L. J. & Sallinger, A. G. Wetting of a chemically heterogeneous surface. *J. Chem. Phys.* **110,** 5969–5975 (1999).
27. Lu, Y. *et al.* Continuous formation of supported cubic and hexagonal mesoporous films by sol-gel dip-coating. *Nature* **389,** 364–368 (1997).
28. Tanev, P. T. & Pinnavaia, T. J. A neutral templating route to mesoporous molecular-sieves. *Science* **267,** 865–867 (1995).
29. Bain, C. D. *et al.* Formation of monolayer films by the spontaneous assembly of organic thiols from solution onto gold. *J. Am. Chem. Soc.* **111,** 321–335 (1989).
30. Cairncross, R. A., Schunk, P. R., Baer, T. A., Rao, R. R. & Sackinger, P. A. A finite element method for free-surface flows of incompressible fluids in three dimensions, Part 1: Boundary-fitted mesh motion. *Int. J. Numer. Meth. Fluids* (in the press).
31. Baer, T. A., Cairncross, R. A., Schunk, P. R., Rao, R. R. & Sackinger, P. A. A finite element method for free-surface flows of incompressible fluids in three dimensions, Part 2: Dynamic wetting lines. *Int. J. Numer. Meth. Fluids* (in the press).
32. Frye, G. C., Ricco, A. J., Martin, S. J. & Brinker, C. J. in *Better Ceramics Through Chemistry III* (eds Brinker, C. J., Clark, D. E. & Ulrich, D. R.) 349–354 (Materials Research Society, Reno, Nevada, 1988).

Supplementary Information is available on *Nature*'s World-Wide Web site (http://www.nature.com) or as paper copy from the London editorial office of *Nature*.

Acknowledgements

We thank R. Assink for performing NMR experiments, P. Yang for technical assistance with micropen lithography, and K. Burns for technical illustrations. TEM investigations were performed in the Department of Earth and Planetary Sciences at the University of New Mexico. Sandia is a multiprogram laboratory operated by Sandia Corporation, a Lockheed-Martin Company, for the US Department of Energy (DOE). This work was supported by the US DOE Basic Energy Sciences Program, the Sandia National Laboratories Laboratory-Directed Research and Development Program, the Defense Advanced Research Projects Agency Bio-Weapons Defense Program, and the US Department of Defense Office of Naval Research.

Correspondence and requests for materials should be addressed to C.J.B. (e-mail: cjbrink@sandia.gov).

Large differences in tropical aerosol forcing at the top of the atmosphere and Earth's surface

S. K. Satheesh & V. Ramanathan

Center for Clouds, Chemistry, and Climate (C^4), Scripps Institution of Oceanography, University of California at San Diego, La Jolla, California 92093 USA

The effect of radiative forcing by anthropogenic aerosols is one of the largest sources of uncertainty in climate predictions[1–6]. Direct observations of the forcing are therefore needed, particularly for the poorly understood tropical aerosols. Here we present an observational method for quantifying aerosol forcing to within ±5 per cent. We use calibrated satellite radiation measurements and five independent surface radiometers to quantify the aerosol forcing simultaneously at the Earth's surface and the top of the atmosphere over the tropical northern Indian Ocean. In winter, this region is covered by anthropogenic aerosols of sulphate, nitrate, organics, soot and fly ash from the south Asian continent[7,8]. Accordingly, mean clear-sky solar radiative heating for the winters of 1998 and 1999 decreased at the ocean surface by 12 to 30 W m^{-2}, but only by 4 to 10 W m^{-2} at the top of the atmosphere. This threefold difference (due largely to solar absorption by soot) and the large magnitude of the observed surface forcing both imply that tropical aerosols might slow down the hydrological cycle.

During December to April of each year, the tropical Indian-Ocean/Atmosphere system acts as a natural experiment for observing the radiative forcing by anthropogenic aerosols[7]. The gaseous and particulate pollutants emitted by the Indian sub-continent and the south Asian region are transported over the entire north Indian Ocean by the persistent northeastern low-level monsoonal flow reaching as far south as 5° to 10° S (refs 7–11). The Indian Ocean Experiment, INDOEX[7], was organized to assess the climatic and chemical influence of anthropogenic aerosols in this region. This focused international experiment has been collecting data from ships, satellites and surface stations since 1996, and culminated in the intensive field phase conducted during January to March 1999.

The Kaashidhoo Climate Observatory (KCO)[7,8], established as part of INDOEX in the island of Kaashidhoo at 4.965° N, 73.466° E about 500 km southwest of the southern tip of India, has been continually measuring the aerosol chemical, radiative and microphysical properties since February 1998. During the winter monsoon, the air mass over KCO mostly (about 90% of the time) originates from the Indian and south Asian sub-continents[11]. Coincident with the KCO observations are the radiation budget data from NASA's Clouds and Earth's Radiant Energy system (CERES) satellite, with an absolute accuracy of 0.2% or better, with a comparable precision[12,13]. The KCO data, along with several ship-borne measurements, have been documented extensively[8–11]. The data have also been used to develop a detailed aerosol–radiation model[8]. Here we compare the results of this model with the observed aerosol forcing. The model simulates the observed surface and TOA solar fluxes to within a few per cent (ref. 8).

The aerosol columnar optical depth at 0.5 μm wavelength (τ_v) ranges from 0.2 to 0.7 and undergoes significant daily, monthly and inter-annual variability (Fig. 1), and is a good index for the overall solar radiative effect of aerosols. The mean value of τ_v shown in Fig. 1 during February–March 1999 was ~0.41 compared to the corresponding value of 0.16 during 1998. The variability is much higher at smaller wavelengths (~0.34 μm) compared to near-infrared wavelengths (~1 μm), indicating that the increase in aerosol optical depth is dominated by sub-micrometre particles typical of anthropogenic sources. The KCO aerosol measurements[8] reveal that sulphate and ammonium are responsible for 29% of the observed optical depth (τ_v), sea-salt and nitrate about 17%, mineral dust about 15%, and the inferred soot, organics, and fly ash contribute respectively 11%, 20% and 8%. The single scattering albedo, ω_0 (where ω_0 = scattering/[scattering + absorption]), for the composite

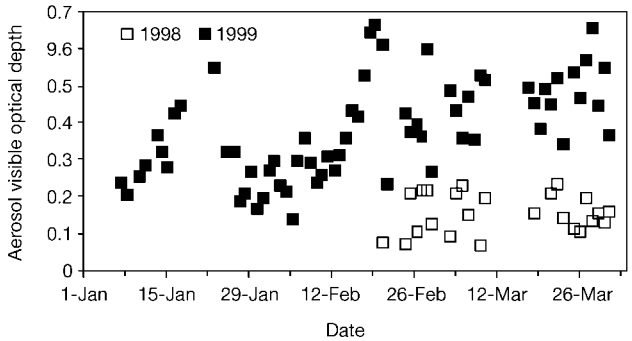

Figure 1 Temporal variation of aerosol optical depth. The figure shows aerosol optical depth at 500 nm wavelength for 1998 (open squares) and 1999 (filled squares). During 1998, the observations are available only during February and March.

aerosol was measured to be consistently in the range of 0.87 to 0.9, regardless of the large fluctuation in optical depths, indicating a highly absorbing aerosol. Anthropogenic sources contribute ~60% or more to the observed optical depths[8].

We employ two methods, method 1 and method 2, for estimating the surface forcing efficiency, f_e^S, to reduce radiometeric uncertainties[14] (see Methods section for radiometers used). In method 1, f_e^S is obtained by subtracting the observed solar flux from that estimated by the model for an aerosol-free atmosphere. The main uncertainty in method 1 is that instrumental offsets or bias in the model will bias the forcing accordingly. In method 2, the aerosol forcing estimated from method 1 is plotted as a function of the observed aerosol optical depth (Fig. 2a). The slope of the forcing versus τ_v yields the aerosol surface forcing efficiency, f_e^S. The value of f_e^S when multiplied by the individual daily value of τ_v yields the aerosol forcing for each day for method 2. The forcing estimated from method 2 is not influenced by instrumental or model offsets.

Several consistency checks assured us of the robustness of the observed f_e^S values of −70 to −75 W m^{-2}. First, these are consistent with modelled values (Fig. 2a), when single-scattering albedos were specified to be within the observed range of 0.87 to 0.9. Second, f_e^S agreed within 5% when obtained separately for the 1998 and 1999 data. The third check comes from the f_e^S obtained from the spectro-radiometer (0.4–1.0 μm), which is about −55 W m^{-2}. When this value is multiplied by the narrow-band to broad-band difference (a factor of ~1.3), it is in excellent agreement with the values in Fig. 2a. Another check is with photodiode radiometer (0.4–0.7 μm) measurements, obtained during the 1996 cruise of ORV *Sagar Kanya*, and which yielded[9] an f_e^S of about −40 W m^{-2} for the northern Indian Ocean. For this value, when multiplied with the modelled ratio of ~1.73 for the broadband to visible (0.4–0.7 μm) values of f_e^S, we obtain −69 W m^{-2}. The similarity between 1996, 1998 and 1999 and between KCO and other regions in the northern Indian Ocean indicate that the KCO forcing efficiency of −70 to −75 W m^{-2} is representative of f_e^S for the tropical Indian Ocean when it is subject to polluted air masses.

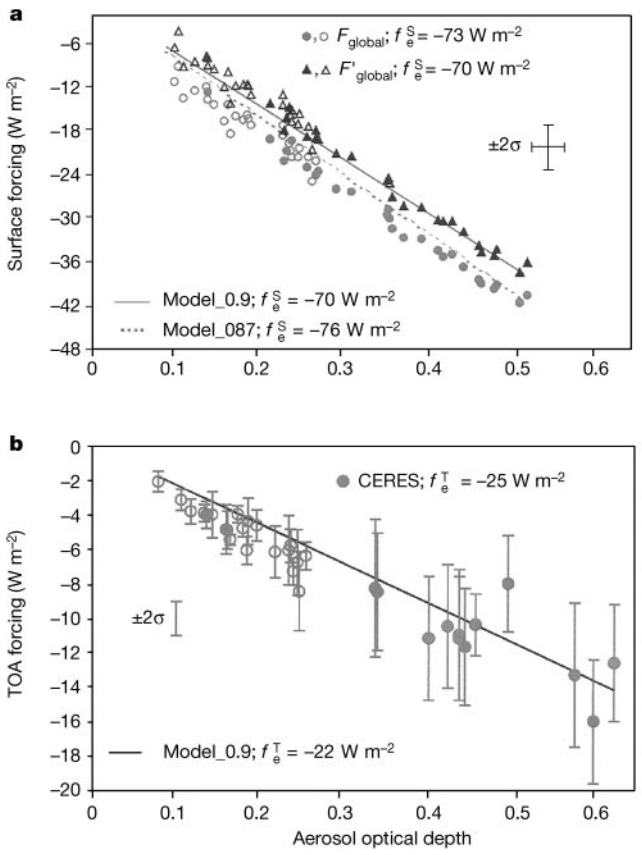

Figure 2 Aerosol forcing in the atmosphere. **a**, The solar aerosol forcing at the Earth's surface (broadband and diurnally averaged) as a function of columnar aerosol optical depth at 500 nm wavelength. The circles correspond to F_{global} (direct + diffuse) and triangles correspond to F'_{global}. Open symbols represent 1998 and solid symbols represent 1999. The vertical and horizontal bars represent the uncertainties in the forcing and optical depths, respectively. The surface forcing efficiency, f_e^S is the slope of the surface forcing with respect to aerosol optical depth. The top of the atmosphere (TOA) forcing efficiency, f_e^T is the slope of the TOA forcing with respect to aerosol optical depth. Model_0.9 and Model_087 represent the modelled value of the forcing efficiencies for aerosol single-scattering albedos of 0.9 and 0.87 respectively. **b**, The solar aerosol forcing at the TOA. The vertical bar represents the pixel-to-pixel variability of the TOA fluxes. Open circles represent 1998 and solid circles represent 1999.

The four independent observations for the monthly mean forcing and the model values are in excellent agreement (Table 1). The aerosols decrease the ocean solar heating by −23 to −37 W m^{-2} which is equivalent to a reduction by 10–15%. The collocated clear-sky forcing at the top of the atmosphere (TOA), estimated from the CERES radiation budget data[15,16], is plotted against aerosol visible optical depths (Fig. 2b) to get TOA forcing efficiency, f_e^T, of about −25 W m^{-2}, which compares well with the model estimate of about −22 W m^{-2}. Our TOA forcing values are also consistent with the Indian Ocean values deduced from the Earth Radiation Budget Experiment data[17]. The decrease of 45–50 W m^{-2} between TOA and surface forcing f_e^T and f_e^S implies absorption of solar radiation in the atmosphere due to aerosols. The ratio f_e^S/f_e^T, an indication of the aerosol absorbing efficiency, is ~3 for the observations (Fig. 2a and 2b) and about 3.4 for the model. A model with just sea-salt or sulphate aerosols will yield a ratio of only 1.5 (refs 17, 18). When soot is removed from the KCO model, the ratio decreases to ~1.9. Thus, although soot contributes only about 10% to τ_v, it strongly affects the surface forcing.

For 1998, the mean forcing values in February and March are: $f^S = -12$ W m^{-2} and $f^T = -4$ W m^{-2}, and the atmospheric forcing, $f^A = f^T - f^S$, is +8 W m^{-2}. The corresponding values for 1999 are: $f^S = -30$ W m^{-2}, $f^T = -10$ W m^{-2} and $f^A = 20$ W m^{-2}. How representative are the large forcing values for the rest of the Indian Ocean?

The high optical depth values shown in Fig. 1 are not unique to KCO. Satellite measurements over the tropical Indian Ocean[19] during the 1998 and 1999 winter months reveal that the northern Indian Ocean has τ_v values exceeding 0.2 for latitudes north of 5° N, and τ_v increases northwards reaching values as high as 0.4 to 0.6 towards the coastal oceans. Ship-borne measurements since 1996 corroborate the satellite data[9,10]. When this is combined with the f_e^S shown in Fig. 2, we infer that the surface solar heating during the winter months may have decreased by as much as 15–40 W m^{-2} over the northern Indian Ocean, and the lower atmospheric solar heating increased by 10–30 W m^{-2}. The atmospheric heating translates into a diurnal mean heating rate perturbation of about 0.3–1 K d^{-1} with 1–3 K d^{-1} during local noon which is an increase of 50–100% of the aerosol-free solar heating.

The large values of negative surface forcing by aerosols and associated atmospheric heating raise several issues. For absorbing aerosols, the surface forcing and the atmospheric forcing are more

Table 1 Comparison of the monthly mean surface aerosol direct forcing

Month	Method	F_{global} flux	F'_{global} flux (W m^{-2})	Model (W m^{-2})
February 1999	Method 1	−28.3	−22.7	−24.1
	Method 2	−24.5	−23.8	
March 1999	Method 1	−37.4	−31.9	−33.3
	Method 2	−34.1	−33.0	

F_{global} is the global flux obtained by adding the direct flux measured by a pyrheliometer and the diffuse flux measured by a shaded pyranometer. F'_{global} is the global flux measured by an unshaded pyranometer. Method 2 is more accurate since it is not influenced by instrumental biases.

relevant climate quantities than the TOA forcing, as also acknowledged elsewhere[3,20]. Next, how would the tropical oceans respond to such a large decrease in surface solar heating? One possibility is that it might decrease the evaporation (since nearly 80% of the radiative heating in the tropics is balanced by evaporation[21]) thus decreasing the intensity of the hydrological cycle. The ocean may also respond by altering its head transport. Another major question is whether the low clouds can sustain the intense soot-induced solar heating, or whether they will burn off. The low-level trade cumulus clouds, north of the inter-tropical convergence zone (ITCZ), are embedded within the aerosol layer (Fig. 3), and the low clouds evaporate when subject to enhanced solar heating[3,22]. Finally, it is uncertain whether the soot-induced heating can modify the monsoonal circulations. This question arises because of the existence of significant north–south gradients in the sooty haze layer across the ITCZ (Fig. 3). Our results raise substantial new questions regarding the regional climate effects.

Lastly, we explore the global significance of the present findings. The large INDOEX surface forcing values are comparable to the $-26\,W\,m^{-2}$ estimated by the Tropospheric Aerosol Radiative Forcing Experiment (TARFOX)[4] for the western North Atlantic Ocean, off the east coast of the United States. Although TARFOX estimates are based on only a few days of aircraft data during July 1996, the close similarity in the surface forcing between the two oceanic regions both downwind of significant anthropogenic sources is striking. Direct forcing observations are too few to make generalizations, but we can speculate from observed aerosol optical properties. Large aerosol concentrations ($\tau_v > 0.15$) in conjunction with absorbing aerosols ($\omega_0 < 0.95$) are required to obtain the large negative surface forcing and f^S/f^T ratio of 3. Absorbing aerosols with $\omega_0 < 0.95$ are typical of biomass burning[5,23], desert dust[24], and soot from fossil-fuel burning[25]. Such emission sources of absorbing aerosols are prevalent in the Northern Hemisphere[25,26]. With respect to fossil-fuel burning, recent ice-core data in western Europe reveals that black carbon concentrations have tripled since early 1850 (ref. 27). Clearly, we are in the early stages of understanding the effects of these sub-micrometre particles on the temperature and the water cycle of the planet. □

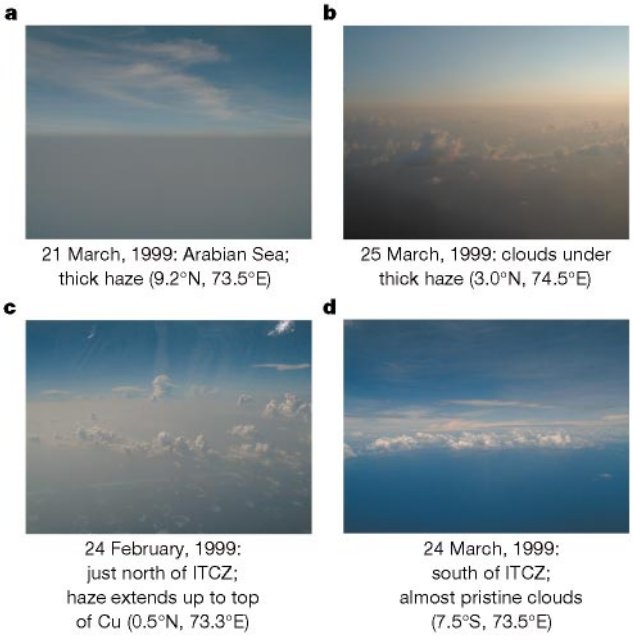

Figure 3 Clouds in the presence of aerosol. Low clouds over the tropical Indian Ocean embedded within the aerosol layer: **a**, **b**, north of the ITCZ; **c**, near the ITCZ; and **d**, free of the haze south of the ITCZ.

Methods

The aerosol optical depths were measured using the CIMEL radiometer of the Aerosol Robotic network (AERONET) of NASA/GSFC as well as a hand-held Microtops radiometer. Because of the inherent uncertainties in the radiometric measurements[14], we used employed two independent broadband instrument sets to obtain the solar irradiance, and two independent analytical techniques to derive the aerosol forcing. In addition, we employed two spectral radiometers to check the broadband instrument results. The direct broadband solar flux (0.2–4 μm) was measured by a Kipp and Zonen pyrheliometer mounted on a Sun tracker. The absolute accuracy of this instrument is $\pm 3\,W\,m^{-2}$, with a precision of about 1% per year. A ventilated Kipp and Zonen pyranometer, shaded from the direct solar beam, measured the diffuse radiation which, when added to the direct solar flux from the pyrheliometer, gave us our best estimate of the global—direct and diffuse—solar flux, denoted by F_{global}. A second independent estimate of the global flux, F'_{global}, was given by an unshaded pyranometer, which measured both the direct and diffuse radiation. The pyranometers have an absolute accuracy of about ±2%. In addition, the error in the total pyranometer due to directional response (that is, the detector responds differently to radiation depending on the incident angle) can be as much as $\pm 10\,W\,m^{-2}$. A spectro-radiometer (Analytical Spectral Devices) measured the global flux at 512 narrow bands from 0.35 to 1.05 μm (ref. 10). We used the bands from 0.4 to 1.0 μm in the present study. A photodiode radiometer (Biospherical Instruments) measured the global flux from 0.4 to 0.7 μm (ref. 9). For the direct forcing, we need fluxes for clear skies which were obtained using procedures documented elsewhere[8,10]. The pyranometers and pyrheliometer were calibrated at Kipp and Zonen, and also at the Climate Monitoring and Diagnostic Laboratory of the National Oceanic & Atmospheric Administration. The calibration coefficients between the two sources agree within 1%, and they changed by less than 0.5% between 1998 and 1999. The direct flux was corrected for the diffuse flux entering the field of view, and the diffuse flux was corrected for the shading ball and the shading arm. The shading ball shades the Sun to enable measurement of the diffuse flux from the sky. The shading arm, which holds the ball, also blocks the diffuse flux. Together this correction is about $6\,W\,m^{-2}$ for overhead Sun and $2\,W\,m^{-2}$ when the solar zenith angle is 60°.

The diurnal average fluxes were obtained by fitting the instantaneous clear-sky flux with a diurnal curve obtained from the aerosol radiation model[8]. The aerosol-free flux was obtained from the radiation model[8], which employed the observed column water vapour, vertical profiles of ozone, pressure and temperature. Observed ocean surface albedos[15] were employed to convert the downward global flux to net (down minus up) flux at the surface.

The TOA measurements were obtained from CERES on board the Tropical Rainfall Measuring Mission[28] satellite which was launched in December 1997. CERES was calibrated pre-launch, and is calibrated routinely within 0.1% using in-orbit flight calibration sources[12]. CERES measures the radiances, which are then converted to fluxes using empirical algorithms[13]. The least uncertainty in these algorithms is shown to be for clear-sky oceanic regions[16], which are the only cases considered in this study. The CERES pixel size is 10 km, and CERES fluxes were collocated each day (within ±20 km; 5 min) with KCO optical depth measurement. Surface instruments were used to choose the clear-sky cases. We followed the same procedure outlined under method 1 and method 2 to estimate the diurnal mean forcing at the TOA.

Received 16 October 1999; accepted 31 March 2000.

1. Charlson, R J. *et al.* Climate forcing by anthropogenic aerosols. *Science* **255**, 423–430 (1992).
2. Houghton, J. T. *et al.* (eds) *Climate Change, 1994: Radiative Forcing of Climate Change and an Evaluation of the IPCC IS92 Emission Scenarios* (Cambridge Univ. Press, Cambridge, 1995).
3. Hansen, J. E. *et al.* Climate forcings in the industrial era. *Proc. Natl Acad. Sci. USA* **95,** 12753–12758 (1998).
4. Russell, P. B. *et al.* Aerosol induced radiative flux changes off the United States mid-Atlantic coast: Comparison of values calculated from sun photometer and in situ data with those measured by air borne pyranometers. *J. Geophys. Res.* **104,** 2289–2308 (1999).
5. Kaufman, Y. J. *et al.* Smoke, Clouds, and Radiation-Brazil (SCAR-B) experiment. *J. Geophys. Res.* **103,** 31783–31808 (1998).
6. Bates, T. S., Huebert, B. J., Gras, J. L., Griffiths, F. B. & Durkee, P. A. International Global Atmospheric (IGAC) Project's first aerosol characterization experiment (ACE 1): Overview. *J. Geophys. Res.* **103,** 16297–16318 (1998).
7. Ramanathan, V. *et al. Indian Ocean Experiment (INDOEX), A Multi-agency Proposal for Field Experiment in the Indian Ocean* (C^4 publication no. 162, Scripps Institution of Oceanography, La Jolla, 1996); also at ⟨http:/www.indoex.ucsd.edu⟩ (1996).
8. Satheesh, S. K. *et al.* A model for the natural and anthropogenic aerosols over the tropical Indian Ocean derived from Indian Ocean Experiment data. *J. Geophys. Res.* **104,** 27421–27440 (1999).
9. Jayaraman, A. *et al.* Direct observations of aerosol radiative forcing over the tropical Indian Ocean during the January–February 1996 pre-INDOEX cruise. *J. Geophys. Res. D* **103,** 13827–13836 (1998).
10. Meywerk, J. & Ramanathan, V. Observations of the spectral clear-sky aerosol forcing over the Tropical Indian Ocean. *J. Geophys. Res.* **104,** 24359–24370 (1999).
11. Krishnamurti, T. N., Jha, B., Prospero, J. M., Jayaraman, A. & Ramanathan, V. Aerosol and pollutant transport and their impact on radiative forcing over tropical Indian Ocean during the January–February, 1996 pre-INDOEX cruise. *Tellus B* **50,** 521–542 (1998).
12. Lee, R. B. *et al.* Pre-launch calibrations of the Clouds and Earth's Radiant Energy System (CERES) tropical rainfall measuring mission and Earth Observing System (EOS): morning (AM-1) spacecraft thermistor bolometer sensors. IEEE. *Trans. Geosci. Remote Sensing* **36,** 1173–1185 (1998).
13. Weilicki, B. A. *et al.* Clouds and the Earth radiant Energy System (CERES): An Earth observing system experiment. *Bull. Am. Meteorol. Soc.* **77,** 853–868 (1996).
14. Bush, B. C., Valero, F. P. J., Simpson, A. S. & Bignone, L. Characterization of thermal effects in pyranometers: A data correction algorithm for improved measurement of surface insolation. *J. Atmos. Ocean. Technol.* (in the press).
15. Breigleb, B. P., Minnis, P., Ramanathan, V. & Harrison, E. Comparison of regional clear-sky albedos inferred from satellite observations and model computations. *J. Clim. Appl. Meteorol.* **25,** 214–226 (1986).

16. Ramanathan, V. *et al.* Cloud radiative forcing and climate: Results from the Earth Radiation Budget Experiment. *Science* **243,** 57–63 (1989).
17. Haywood, J. *et al.* Tropospheric aerosol climate forcing in clear-sky satellite observations over the oceans. *Science* **283,** 1299–1303 (1999).
18. Coakley, J. A. & Cess, R. D. Response of the NCAR community climate model to the radiative forcing by the naturally occurring tropospheric aerosol. *J. Atmos. Sci.* **42,** 1677–1692 (1985).
19. Rajeev, K., Ramanathan, V. & Meywerk, J. Regional aerosol distribution and its long range transport over the Indian Ocean. *J. Geophys. Res.* **105,** 2029–2043 (2000).
20. Cess, R. D. *et al.* Climatic effects of large injections of atmospheric smoke and dust—A study of climate feedback mechanisms with one-dimensional and 3-dimensional climate models. *J. Geophys. Res.* **90,** 2937–2950 (1985).
21. Hartman, D. L. *Global Physical Climatology* (Academic, San Diego, 1994).
22. Ackerman, A. S. *et al.* Reduction of tropical cloudiness by soot. *Science* (in the press).
23. Penner, J. E., Dickerson, R. E. & Oneill, C. A. Effects of aerosol from biomass burning on the global radiation budget. *Science* **256,** 1432–1434 (1992).
24. Tegen, I., Lacis, A. A. & Fung, I. The influence on climate forcing of mineral aerosols from disturbed soils. *Nature* **380,** 419–422 (1996).
25. Cooke, W. F. *et al.* Construction of a 1 degrees × 1 degrees fossil fuel emission data set for carbonaceous aerosol and implementation and radiative impact in the ECHAM4 model. *J. Geophys. Res.* **104,** 22137–22162 (1999).
26. Prospero, J. M. & Nees, R. T. Impact of the north African drought and El-Nino on mineral dust in the Barbados trade winds. *Nature* **320,** 735–738 (1986).
27. Lavanchy, V. M. H., Gaggeler, H. W., Schotterer, U., Schwikowski, M. & Baltensperger, U. Historical record of carbonaceous particle concentrations from a European high-alpine glacier (Colle Gnifetti, Switzerland). *J. Geophys. Res.* **104,** 21227–21236 (1999).
28. Theon, J. S. The Tropical Rainfall Measuring Mission (TRMM). *Adv. Space Res.* **14,** 159–165 (1993).

Acknowledgements

We thank the Government of Maldives for providing the land for KCO and for assistance in its operation. We also thank B. N. Holben for providing the AERONET data, and K. Priestley and N. Loeb for the CERES data. The US component of INDOEX is funded by the NSF and the US Department of Energy, and KCO was funded by the NSF and the Vetlesen Foundation. We also thank J. Fein for providing support to both INDOEX and KCO.

Correspondence and requests for materials should be addressed to V.R. (e-mail: ram@fiji.ucsd.edu).

Sensitivity of the geomagnetic axial dipole to thermal core–mantle interactions

Jeremy Bloxham

Department of Earth and Planetary Sciences, Harvard University, Cambridge, Massachusetts 02138, USA

Since the work of William Gilbert in 1600 (ref. 1), it has been widely believed that the Earth's magnetic field, when suitably time-averaged, is that of a magnetic dipole positioned at the Earth's centre and aligned with the rotational axis. This 'geocentric axial dipole' (GAD) hypothesis has been the central model for the study of the Earth's magnetic field—it underpins almost all interpretations of palaeomagnetic data, whether for studies of palaeomagnetic secular variation, for plate tectonic reconstructions, or for studies of palaeoclimate[2]. Although the GAD hypothesis appears to provide a good description of the Earth's magnetic field over at least the past 100 Myr (ref. 2), it is difficult to test the hypothesis for earlier periods, and there is some evidence that a more complicated model is required for the period before 250 Myr ago[3]. Kent and Smethurst[3] suggested that this additional complexity might be because the inner core would have been smaller at that time. Here I use a numerical geodynamo model and find that reducing the size of the inner core does not significantly change the character of the magnetic field. I also consider an alternative process that could lead to the breakdown of the GAD hypothesis on this timescale, the evolution of heat-flux variations at the core–mantle boundary, induced by mantle convection. I find that a simple pattern of heat-flux variations at the core–mantle boundary, which is plausible for times before the Mesozoic era, results in a strong octupolar contribution to the field, consistent with previous findings[3].

To test the GAD hypothesis directly it is necessary to have palaeomagnetic measurements from known palaeolatitudes (the original latitudes at the time of acquisition of the remanent magnetization which will have changed because of plate tectonics and true polar wander). Then, the palaeomagnetic inclination (I) can be compared with that which would result from a GAD field. Palaeolatitude can be determined for roughly the past 150 Myr from plate reconstructions made using the pattern of magnetic stripes on the sea floor, a process which is largely independent of the validity of the GAD model. Earlier than 150 Myr ago, there is little remaining sea floor, and plate reconstructions become much less complete, so the palaeolatitudes of the samples are poorly determined. Determination of palaeolatitude must then resort to such proxies as palaeoclimate[4]. Although general agreement is found between these proxies and the GAD model[2], the latitudinal resolution of climate proxies is very limited and departures from the GAD configuration are possible.

An alternative approach to testing the GAD hypothesis is to examine the frequency distribution of $|I|$ (ref. 5). Instead of attempting a test on a site-by-site basis, all the measurements are compiled and a histogram is plotted of frequency versus $|I|$. In a similar vein, here I compare the palaeomagnetic inclination measurements with the cumulative distribution function (c.d.f.) for $|I|$ derived from the GAD model.

In Fig. 1, I compare the $|I|$ c.d.f. for the GAD model with palaeomagnetic measurements from the Global Paleomagnetic Data Base[6] separated into two time intervals: the Cenozoic and Mesozoic eras (0–250 Myr ago), from which we have selected 3,655 measurements; and the Palaeozoic era and Precambrian time (earlier than 250 Myr ago), from which we have selected 3,503 measurements. We exclude any measurements which are clearly the result of secondary magnetizations. The more recent data conform fairly closely to the GAD model, though with a small deficit of low inclinations. On the other hand, the earlier data show a strong bias towards low inclinations, as previously noted[3]. A simple measure of this distinction is provided by the median of $|I|$: earlier than 250 Myr ago it is 31°; later than 250 Myr ago it is 48°; and for the GAD model it is 49°.

Several possible explanations have been proposed for the misfit of the older data to the GAD model, including sampling biases, palaeomagnetic artefacts, and departures of the geomagnetic field from the GAD configuration. Kent and Smethurst[3] showed that a departure of the field from the GAD configuration in the form of an axial octupole term (of the same sign as the axial dipole and about 25% of its strength) results in a distribution of $|I|$ more closely resembling that from earlier than 250 Myr ago, though they were not able to dismiss other explanations. They proposed that this field configuration may have resulted because the inner core was smaller then than it is at present.

I tested their proposal using a numerical dynamo model. In Fig. 1, I show $|I|$ calculated using a dynamo model[7] with the Earth's current inner-core radius (approximately 1,200 km) and with a radius 25% smaller. The smaller radius corresponds to a time roughly 1,000 Myr to 2,000 Myr ago depending on the heat flux across the core–mantle boundary[8]. Both the Earth's current inner-core radius and the smaller inner-core radius give distributions which closely match that of the GAD configuration. I conclude from this that the growth of the inner core does not seem to provide an explanation for possible octupolar contributions to the field earlier than 250 Myr ago. Furthermore, my test is conservative in the sense that an inner-core radius has been chosen which represents a time much longer ago that represented by the bulk of the observations from earlier than 250 Myr ago.